J. Fluid Mech. (2004), *vol.* 504, *pp.* 239–270. © 2004 Cambridge University Press
DOI: 10.1017/S0022112004008274 Printed in the United Kingdom

A study of shock waves in expanding flows on the basis of spectroscopic experiments and quasi-gasdynamic equations

By I. A. GRAUR[1], T. G. ELIZAROVA[1], A. RAMOS[2], G. TEJEDA[2], J. M. FERNÁNDEZ[2] and S. MONTERO[2]†

[1]Institute for Mathematical Modeling, RAS Miusskaya Sq., 4a, 125047 Moscow, Russia
[2]Instituto de Estructura de la Materia, CSIC Serrano 121, 28006 Madrid, Spain

(Received 24 April 2003 and in revised form 20 October 2003)

A comprehensive numerical and experimental study of normal shock waves in hypersonic axisymmetric jets of N_2 is presented. The numerical interpretation is based on the quasi-gasdynamic (QGD) approach, and its generalization (QGDR) for the breakdown of rotational–translational equilibrium. The experimental part, based on diagnostics by high-sensitivity Raman spectroscopy, provides absolute density and rotational temperatures along the expansion axis, including the wake beyond the shock. These quantities are used as a reference for the numerical work. The limits of applicability of the QGD approach in terms of the local Knudsen number, the influence of the computational grid on the numerical solution, the breakdown of rotation–translation equilibrium, and the possible formation of a recirculation vortex immediately downstream from the normal shock wave are the main topics considered.

1. Introduction

Shock waves associated with the two-dimensional axisymmetric expansion of a gas show, more or less modified, many of the well-known peculiarities of the one-dimensional expansion, for instance the sharp density and temperature gradients across the normal shock wave, the breakdown of the thermodynamic equilibrium between translation and rotation degrees of freedom, the lag between the profiles of density, translational temperature and rotational temperature, the thermal overshoot at the end of the shock wave, and the bimodal distribution of temperatures across it. In addition, a characteristic of two-dimensional axisymmetric supersonic expansions seems to be a recirculation vortex associated with the normal shock wave, which has been mentioned incidentally in several recent works (Chen, Chakravorty & Hung 1994; Stenholm & Jover 1997; Welsh 1997; Gribben *et al.* 1998; Frey & Hagemann 1998; Maté *et al.* 2001). Somewhat more systematic numerical studies of the vortex problem have been acomplished in the framework of the Euler equations by Goryainov (2000), and of the quasi-gasdynamic equations by Graur *et al.* (2002*b*).

In the last decade, the quasi-gasdynamic (QGD) system of equations, and their generalization (QGDR) for the breakdown of the translational–rotational equilibrium, have been employed to calculate flow properties of several gasdynamic systems (Elizarova *et al.* 1995, 1997; Elizarova & Chirokov 1999; Elizarova, Graur & Lengrand

---

† Author to whom correspondence should be addressed: emsalvador@iem.cfmac.csic.es

2001; Graur, Elizarova & Lengrand 1997, 1999; Graur *et al.* 2002*b*; Lengrand *et al.* 1995). These equations constitute a promising gasdynamic approach beyond the Navier–Stokes equations. However, the lack of quantitative experimental data to compare with has left open a number of relevant questions about the limits of applicability of the QGD approach in highly demanding computational problems like the two-dimensional shock waves. Among them, a major one is to what extent several 'difficult' flow fields can be calculated accurately with the same method.

In this paper we present a comprehensive numerical and experimental study of the two-dimensional problem of the shock wave and associated vortex formation in axisymmetric jets of N_2. The experimental part concerns the properties of five normal shock waves in axisymmetric expansions of N_2 generated under different stagnation-to-background pressure ratios. These ratios were chosen to produce normal shock waves differing considerably in their properties, spanning a range of Mach numbers $7.7 < M < 15.3$, reaching maximum values of local Knudsen numbers $0.33 < Kn < 0.59$ within the shock wave. The absolute density profiles and the rotational temperature profiles of these five shock waves have been measured with unprecedented accuracy and spatial resolution by means of high-sensitivity Raman spectroscopy using the miniature jet diagnostic facility at the Instituto de Estructura de la Materia (Montero *et al.* 2000, Ramos *et al.* 2000).

The numerical interpretation is based on the QGD approach, and on its QGDR generalization for the breakdown of the translational–rotational equilibrium, particularly severe at the shock wave. The experimental material, rich in density–temperature features, provides a firm basis to test the capability of QGD and QGDR modelling of shock waves which are in the continuum limit by virtue of their large local Knudsen numbers. In particular, the present flow fields are characterized by the following difficulties: (*a*) a wide range of local Knudsen numbers, with experimental values in the range $Kn < 0.59$; (*b*) gasdynamic quantities (pressure, temperature, flow velocity) varying by several orders of magnitude, with strong local gradients; and (*c*) high rarefaction, and severe breakdown of rotational–translational equilibrium in some local regions. Such high values of the local Knudsen number imply a limit to the continuum models associated with the breakdown of the Maxwellian distribution, while the breakdown of translational–rotational equilibrium poses the problem of the rotational distribution function. In QGD and QGDR approaches this distribution function is based on a continuous distribution of rotational energy, while the molecular rotational quantum energies are of discrete nature, markedly departing from a continuum at the low local temperatures reached at the onset of the present shock waves, on the order of 10 K.

Testing different computational variants under these limit conditions, with emphasis on the topics enumerated above, is the main target of the present work. Another question that has received our attention is the formation of vortices beyond the shock waves, akin to those described in the recent literature. The merits of the QGDR generalization, compared with the plain QGD approach, and the use of multiprocessor systems in connection with very fine computational grids are also treated in some detail.

The paper is structured as follows. In § 2, the theoretical background of the QGD and QGDR equations is presented, with emphasis in the differences with the Navier–Stokes equations. The experimental aspects of the shock waves studied are described in § 3. Computational and numerical treatment of the QGD and QGDR equations is given in § 4. A discussion of the density, temperature, and velocity profiles of the five shock waves, calculated with different approximations, is presented in § 5, including comparison with experiment where possible. The numerical results and the vortex problem are discussed in § 6. Finally, the conclusions are summarized in § 7. Appendices A and B include details of the QGD equations adapted to axial symmetry, and its vectorial representation for numerical calculations.

2. Theory

2.1. *The QGD and QGDR equations*

The quasi-gasdynamic (QGD) equations, originally developed by Elizarova & Chetverushkin (1984, 1988) on the basis of a kinetical model of the distribution function, are reputed to produce robust numerical algorithms suited for the calculation of viscous supersonic flows. For the stationary case, the Navier–Stokes (NS) equations are the asymptotic limit of the QGD equations when the Maxwellian relaxation time τ tends to zero. This property can easily be deduced from the formulation of the QGD equations presented below.

In the domain of small Knudsen numbers where the NS equations are accepted to be valid, the QGD equations do not distort the NS solution but just stabilize the numerical algorithm. In this case, QGD, NS, and direct simulation Monte Carlo (DSMC) results, tend to coincide as has been shown by Elizarova *et al.* (1995, 1997), and are in good general agreement with the experimental results (Graur *et al.* 2003). For larger Knudsen numbers, QGD results have proved to be superior to NS results, compared with experiment in microchanneles (Elizarova & Sheretov 2002). QGD calculations, though less accurate than DSMC calculations, are considerably cheaper from the computational point of view, and appear to be better suited for problems where the gasdynamic properties span a range of several orders of magnitude, like in the jets and shock waves studied in the present work.

Gasdynamic structures may be described by a system of three differential equations accounting for

conservation of mass (continuity equation)

$$\frac{\partial \rho}{\partial t} + \nabla_i J^i = 0, \tag{1}$$

momentum

$$\frac{\partial (\rho u^k)}{\partial t} + \nabla_i J^i u^k + \nabla^k p = \nabla_i \Pi^{ik}, \tag{2}$$

and total energy

$$\frac{\partial E}{\partial t} + \nabla_i \frac{J^i}{\rho}(E + p) + \nabla_i q^i = \nabla_i (\Pi^{ik} u^k), \tag{3}$$

where the macroscopic flow quantities are ρ (density), u_i (velocity coordinates), p (pressure), and E (total energy per unit volume).

Different choices for the mass flux vector J^i, the shear-stress tensor Π^{ik}, and the heat flux vector q^i, lead either to the NS equations, or to the QGD equations used below (Sheretov 1997, 2000). The Navier–Stokes equations are derived from

$$J^i = J^i_{NS} = \rho u^i, \tag{4}$$

$$\Pi^{ik} = \Pi^{ik}_{NS} = \mu[\nabla^k u^i + \nabla^i u^k - (2/3) g^{ik} \nabla_j u^j] + \zeta g^{ik} \nabla_j u^j, \tag{5}$$

$$q^i = q^i_{NS} = -\kappa \nabla^i T, \tag{6}$$

where μ is the viscosity, g^{ik} is the metric tensor, ζ is the bulk viscosity, and $\kappa = c_p\mu/Pr$ is the heat conductivity; Pr is Prandtl number, and $\gamma = c_p/c_v$ the ratio of heat capacities; ζ has been taken as $\zeta = \mu(5/3 - \gamma)$ according to Elizarova & Chirokov (1999). The gasdynamic variables ρ, u_i, and p involved are instantaneous space-averaged quantities. In contrast to the Navier–Stokes equations, if the gasdynamic quantities ρ, u_i, and p are defined by means of time–space averaging (instead of space averaging), the system (1)–(3) can be closed in the QGD approach by

$$J^i = J^i_{NS} + J^i_D, \quad J^i_D = -\tau[\nabla_j(\rho u^i u^j) + \nabla^i p], \tag{7}$$

$$\Pi^{ik} = \Pi^{ik}_{NS} + \Pi^{ik}_D, \quad \Pi^{ik}_D = \tau u^i[\rho u^j \nabla_j u^k + \nabla^k p] + \tau g^{ik}[u_j \nabla^j p + \gamma p \nabla_j u^j], \tag{8}$$

$$q^i = q^i_{NS} + q^i_D, \quad q^i_D = -\tau\rho u^i[u^j\nabla_j\varepsilon + p u_j \nabla^j(1/\rho)], \tag{9}$$

where $\tau = \mu/p$ is the averaging time, chosen to be equal to the Maxwellian relaxation time, and $\varepsilon = p/(\rho(\gamma - 1))$; $(\ )_D$ stands for the dissipative terms additional to the Navier–Stokes contributions referred to as $(\ )_{NS}$ (Sheretov 1997, 2000).

The QGDR equations were developed by Elizarova & Chirokov (1999) as a generalization of the QGD equations. The QGDR equations for a gas with three translational and two rotational degrees of freedom, with $\gamma = 7/5$, are intended to account for the non-equilibrium $T_{tr} \neq T_{rot}$ between translational and rotational temperatures. The QGDR equations can be written like the QGD ones, with equations (1) and (2) retaining their form, while in (7) and (8) p is replaced by p_{tr}, and τ by $\tau_{tr} = \mu/p_{tr}$, with the viscosity $\mu = \mu(T_{tr})$ only depending on the translational temperature. In turn, the energy equation (3) is split in the QGDR generalization into one equation for the translational energy E_{tr} per unit volume,

$$\frac{\partial E_{tr}}{\partial t} + \nabla_i \frac{J^i}{\rho}(E_{tr} + p_{tr}) + \nabla_i q^i_{tr} = \nabla_i(\Pi^{ik}u^k) + S_{tr}, \tag{10}$$

and another equation for the rotational energy E_{rot} per unit volume,

$$\frac{\partial E_{rot}}{\partial t} + \nabla_i u^i E_{rot} + \nabla_i q^i_{rot} = \nabla_i \tau \nabla_j u^i u^j E_{rot} + \nabla_i \tau \frac{p_{rot}}{\rho} \nabla^i p_{tr} + S_{rot}, \tag{11}$$

with

$$E_{tr} = \frac{\rho(u^i)^2}{2} + \frac{p_{tr}}{\gamma - 1}, \quad E_{rot} = p_{rot}, \tag{12}$$

and S_{tr} and S_{rot} the energy exchange terms defined below.

The total heat flux q^i is also split into the partial contributions

$$q^i_{tr} = -\frac{1}{Pr}\frac{5}{2}\mu\nabla^i\frac{p_{tr}}{\rho} - \tau\rho u^i[u^j\nabla_j\varepsilon + p_{tr}u_j\nabla^j(1/\rho)], \tag{13}$$

where $\varepsilon = p_{tr}/(\rho(\gamma - 1))$, responsible for the heat conduction due to the gradient of translational temperature T_{tr} , and

$$q^i_{rot} = -\frac{1}{Pr}\mu\nabla^i\frac{p_{rot}}{\rho}, \tag{14}$$

for the heat conduction due to the gradient of rotational temperature T_{rot}. Note that in the QGDR model both heat flux vectors, q_{tr} and q_{rot} in (13) and (14), are proportional to $\mu(T_{tr})$. The viscosity has been treated within the variable hard sphere

(VHS) model, which leads to a thermal dependence

$$\mu = \mu_{ref} \left(\frac{T}{T_{ref}} \right)^{\omega}. \tag{15}$$

The VHS molecular diameter of N_2 employed in the present calculations is $d_{ref} = d(T_{ref}) = 4.17 \times 10^{-10}$ m, while $\mu_{ref} = \mu(T_{ref}) = 1.656 \times 10^{-5}$ N s m^{-2} at $T_{ref} = 273$ K, and $\omega = 0.74$ (Bird 1994).

The energy exchange terms

$$S_{tr} = -S_{rot} = \frac{3}{5\tau_{rot}}(p_{rot} - p_{tr}), \tag{16}$$

in (10) and (11) involve the rotational relaxation time τ_{rot}. Here it has been estimated as $\tau_{rot} = Z\tau_c$, where $\tau_c = \tau(7 - 2\omega)(5 - 2\omega)/30$ is the mean collisional time, and

$$Z = \frac{Z^{\infty}}{1 + \left(\pi^{3/2}/2\right)(T^{\star}/T_{tr})^{1/2} + (\pi + \pi^2/4)(T^{\star}/T_{tr})}, \tag{17}$$

the so-called rotational collision number (Parker 1959); for N_2, the parameters $Z^{\infty} = 23$, and $T^{\star} = 91.5$ K, have been taken from Bird (1994).

Average pressure p_{av} and temperature T_{av} derived from the QGDR generalization, to be compared to the homologous QGD quantities p and T, are defined by

$$p_{av} = (3\, p_{tr} + 2\, p_{rot})/5 = \rho\, (\mathscr{R}/\mathscr{M})\, T_{av}, \tag{18}$$

where $\mathscr{R} = 8.31451$ J K^{-1} mol^{-1} is the universal gas constant, and $\mathscr{M}$ the molar mass of N_2. At thermal equilibrium $p_{tr} = p_{rot} = p_{av} = p$, resulting

$$E = E_{tr} + E_{rot} = \frac{\rho u_i^2}{2} + \frac{p}{\gamma - 1}, \tag{19}$$

for the total energy per unit volume, the QGDR system becoming a single-temperature QGD system with perfect-gas specific heat ratio $\gamma = 7/5$ and Prandtl number $Pr = 14/19$.

The QGD equations in r, z coordinates adapted to the axial symmetry of the present problem are given explicitly in Appendix A. In the present formulation the NS-dissipative terms, $(\ )_{NS} \propto \mu$, (equations (A 7), Appendix A), and the additional dissipative terms, $(\ )_D \propto \tau$, (equations (A 5), (A 6), (A 8), Appendix A) are written separately. For stationary flows the terms in τ have asymptotic order of $O(\tau^2)$ for $\tau \to 0$ or, in the dimensionless form $O(Kn^2)$ (Sheretov 2000).

3. Experimental

Recent progress in instrumentation for high-sensitivity Raman spectroscopy, combined with the design and implementation of suitable expansion chambers, has provided a powerful diagnostic tool for the quantitative investigation of supersonic jets and associated phenomena (Montero *et al.* 2000, 2002; Ramos *et al.* 2000; Maté *et al.* 2001).

Using the facility at the Instituto de Estructura de la Materia (CSIC), the density and rotational temperature profiles of five axisymmetric expansions of N_2 and their normal shock waves, including downstream wakes, have been investigated with high accuracy and spatial resolution. These expansions were generated through a circular nozzle of exit radius $r_e = 0.1565$ mm and internal length ≈1 mm, at room temperature $T_0 = 295$ K, and fixed nominal stagnation pressure of ≈1 bar. Due to the miniature size of the facility, this reference pressure was measured with a pressure transducer connected with the nozzle prechamber by a long and narrow duct. Thus it is just an orientative nominal pressure reference. The actual pressure in the nozzle prechamber, $P_0 = 732$ mbar ($\pm 10\%$), was determined by spectroscopic measurement of the absolute number density at different points of the expansion, some of them very close to the nozzle, extrapolating the fitted function to the nozzle origin located about one nozzle radius inside the nozzle channel (Ramos 2001).

For the conditions mentioned above the expansions are free from any detectable condensation. The five shock waves, henceforth denoted by A, B, C, D, and E, were formed at distances from the nozzle $L = 2.7$, 6.1, 8.5, 11.6, and 15.2 mm by setting the residual pressure in the expansion chamber to $P_\infty = 4.2$, 1.0, 0.5, 0.28, and 0.18 mbar, respectively, by means of an inlet needle valve, always maintaining the same nozzle prechamber pressure of $P_0 = 732$ mbar.

Referred to the critical conditions at the nozzle exit (Mach number $M = 1$) the Reynolds number $Re_e = 2r_e^{eff} u_e \rho_e / \mu_e$ of the investigated expansions is $Re_e \approx 3200$. The flow regime in the mixing layer at the beginning of the expansions can be characterized by a Reynolds number referred to the distance L between nozzle and Mach disk, defined as $Re_L = Re_e / \sqrt{P_0/P_\infty}$ (Volchkov *et al.* 1973; Novopashin & Perepelkin 1989): for $Re_L > 10^4$ the flow is turbulent, the range $10^3 < Re_L < 10^4$ corresponds to the laminar–turbulent transition, for $10^2 < Re_L < 10^3$ the flow is laminar, and in flows with $Re_L < 10^2$ the effects of rarefaction influence the gasdynamic structure. For expansions A to E respectively $Re_L = 243$, 119, 84, 63, and 50, meaning that the flow in expansions A and B is laminar, while in expansions C, D, and E there is increasingly rarefied flow where the gasdynamic structure may be expected to be progressively influenced.

With aid of the expression for the discharge coefficient C_D in terms of Re_e (Benedict 1966; Sreekanth, Prasad & Prasad 1991) we obtain for the present experiments a discharge coefficient $C_D \approx 0.90$. As shown below, this departure from ideal isentropic conditions is consistent with a reduction of the nozzle radius from its nominal value $r_e = 0.1565$ mm to an effective radius $r_e^{eff} \approx 0.148$ mm. These facts, indicative of the departure from the ideal source conditions, may add some degree of quantitative uncertainty to the comparison between numerical and experimental results, but are not sufficiently important to affect seriously the general conclusions on the structure and quantitative properties of the fairly different shock waves and wakes investigated here.

As a guide for the forthcoming dicussion a QGD numerical schlieren picture of the global structure of expansion B is depicted in figure 1(*a*) showing the representative zones of the flow field, which are common to the five expansions A to E, but differ quantitatively. Immediately downstream from the nozzle is the *zone of silence*, the supersonic core where the velocity flow field is nearly radial, with rapid decreasing density and temperature, and increase of flow velocity approaching its asymptotic (terminal) value, followed by the *normal shock wave*, of width δ, where the flow field is sharply deflected outwards from the symmetry axis, with strong decreasing of the flow velocity. The normal shock wave is characterized by a sharp increase of density and temperature across it, and by a marked breakdown of the translational–rotational thermal equilibrium. The final section of the normal shock wave merges with a rethermalized zone of slow subsonic flow velocity. According to some computational results a toroidal *trapped vortex*, displaying negative axial flow velocity, is formed there. This is indeed a controversial region because of the extremely slow flow velocity, hardly amenable to unambiguous experimental conclusions. Beyond this region the

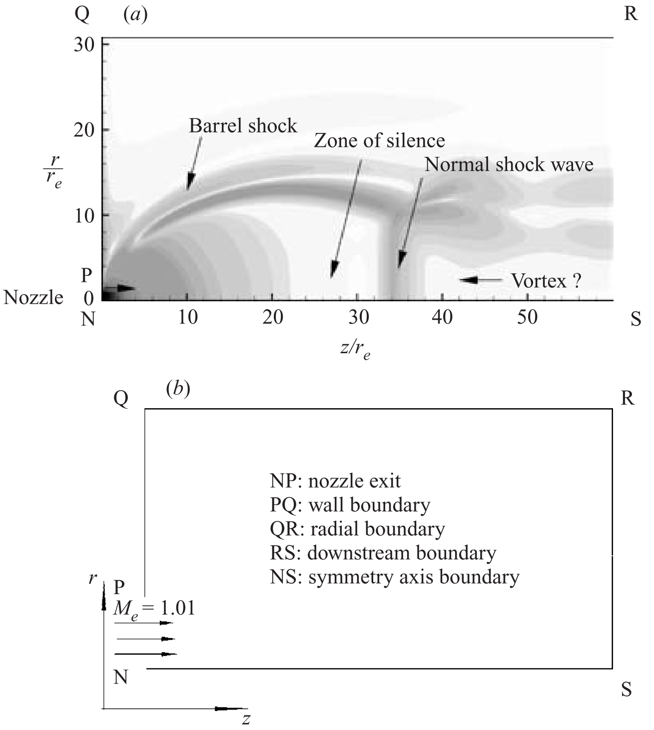

FIGURE 1. Expansion B: (*a*) QGD numerical schlieren picture of expansion B, variant *s*10, (*b*) and the computational domain.

flow field is nearly sonic and tends to collimate parallel to the symmetry axis. The zone of silence, normal shock wave, and supposed vortex are confined by the *barrel shock*, almost rethermalized and of comparatively high density, with slightly supersonic flow velocity. Outside the barrel shock, close to it the flow is slow and probably turbulent, while at distance large enough the gas may be considered at rest at the background pressure p_∞. A thorough description of the general properties of free jets has been given by Volchkov *et al.* (1973), and by Rebrov (1985), while a quantitative mapping of a real free jet of CO_2 has been reported by Maté *et al.* (2001).

The region experimentally investigated here in detail is the axial path of figure 1(*a*). The two-dimensional QGD and QGDR calculations span a computational domain, shown in figure 1(*b*), large enough to include the complete structure of the jet in all five cases A to E.

The experimental spatial resolution at the datapoints probed along the axis of the expansion of figure 1 amounts about 10 μm, equivalent to 0.0638 nozzle radius. This value is far smaller than the experimentally determined widths of the shock waves, $\delta_A = 0.606$, $\delta_B = 2.556$, $\delta_C = 4.920$, $\delta_D = 6.912$, and $\delta_E = 10.480$ also expressed in units of the nozzle radius r_e, and allows the determination of truly local properties even under strong gradient conditions. In terms of mean free path, more meaningful from the physical point of view, the five shock waves display a remarkably constant thickness, with avearage value $\overline{\delta} = (4.37 \pm 0.38)\lambda_1$; δ is defined here according to Bird (1994), and λ_1 is the mean free path at the minimum density point upstream of each shock wave (Ramos *et al.* 2000).

Computational variant	Grid $N_z \times N_r$	z-step h_z/r_e	r-step h_r/r_e	Domain size (mm)
$s1$	$140 \times 92cv$	1	0.1	21.91×15.65
$s2$	$281 \times 92cv$	0.5	0.1	21.91×15.65
$s3$	$561 \times 92cv$	0.25	0.1	21.91×15.65
$s4$	$1401 \times 1001u$	0.1	0.1	21.91×15.65
$s5$	$34 \times 60cv$	1	0.1	5.32×3.14
$s6$	$137 \times 201u$	0.25	0.1	5.32×3.14
$s7$	$171 \times 201u$	0.2	0.1	5.32×3.14
$s8$	$340 \times 201u$	0.1	0.1	5.32×3.14
$s9$	$76 \times 74cv$	1	0.1	11.73×7.84
$s10$	$751 \times 501u$	0.1	0.1	11.73×7.84

TABLE 1. Computational variants used in the present work; u denotes uniform grids and cv constant-variable grids.

The experimental density and rotational temperature profiles of shock waves A, B, C, D, and E, are discussed below, jointly with their QGD or QGDR calculated counterparts under different computational conditions. More details about the procedure for measuring of densities and rotational temperatures in the jet, as well as other features of these shock waves have been reported by Ramos *et al.* (2000).

4. Numerical details

The computational domain of figure 1(b) is covered by a rectangular grid with radial steps h_r, and axial steps h_z. Since the choice of grid and the size of the domain have a determining influence on specific features of the calculated flow fields, in particular on the supposed vortex beyond the normal shock waves, several computational variants, listed in table 1, have been tested.

Two sorts of grids were used, namely (i) uniform grids marked u in table 1 where the step in the axial (z) and radial (r) directions remains constant, and (ii) constant-variable grids marked cv in table 1 where the step size remains constant along the axial direction, while for the radial direction it remains constant for $r < r_e$, but for $r > r_e$ the step increases progressively between adjacent cells with a stretching factor 1.05.

The numerical computation of the QGD and QGDR equations for expansions A to E has been carried out according to a finite-difference scheme where the spatial derivatives are approximated with the centred derivatives (centred scheme). Under high Mach numbers the numerical solution of the QGD and QGDR systems may lead to oscillations in regions with strong gradients in the dynamical variables. To overcome this numerical problem the relaxation time τ is replaced in the dissipative terms, except in those with mixed spatial derivatives, by

$$\tau = \mu/p + \tau_{eff}, \qquad \text{with} \quad \tau_{eff} = \frac{h}{c}\beta, \tag{20}$$

where c is the velocity of sound; the damping parameter β, usually in the range $0.1 < \beta < 0.5$, is given the smallest value that ensures the stability of the solution. This makes the order of the space accuracy of the resulting numerical algorithm equal to $O(\beta h)$. (See Appendix B for the details.)

M_e	1.01	Kn_e	1.09×10^{-4}
T_e	249.2 K	$\tilde{\lambda}_e = \lambda_e/(2r_e)$	3.75×10^{-4}
p_e	0.382 bar	T_∞/T_e	200/249.2
n_e	1.1114×10^{25} m^{-3}	p_∞/p_e	(A) 0.0110
ρ_e	0.517 kg m^{-3}		(B) 0.00262
u_e	325.0 m s^{-1}		(C) 0.00131
μ_e	15.47×10^{-6} s Pa		(D) 0.000732
λ_e	11.73×10^{-8} m		(E) 0.000471

TABLE 2. Nozzle exit quantities of the N_2 jets employed in the QGD and QGDR numerical calculations; $Kn_e = (\lambda_e/n_e)(\mathrm{d}n/\mathrm{d}z)_e$.

The system of finite-difference equations associated with the QGD and QGDR equations is solved here by means of an explicit algorithm where the steady-state solution is attained as the limit of a time-evolving process. The computation finishes when the steady-state solution is reached according to the criterion

$$\frac{1}{N_r N_z} \sum \left| \frac{\rho^{j+1} - \rho^j}{\rho^j \Delta \tilde{t}} \right| \leqslant \epsilon, \tag{21}$$

where the sum is over all computational nodes in the grid; ρ is the density, j the time-step index, N_r, N_z the number of nodes in the r- and z-directions respectively, and $\Delta\tilde{t}$ the dimensionless time step defined as $\Delta\tilde{t} = (c_e/\lambda_e)\Delta t$, where λ_e is the mean free path at the nozzle exit. Here Δt is chosen according to the stability criterion $\Delta t = 0.005 \min(h/c)$. Representative time steps and the number of iterations required for a stationary solution in a QGDR calculation of shock waves A to E (variant $s2$) are: $\epsilon \approx 10^{-8}$, $N_{iter} \approx 5 \times 10^6$, and $\Delta\tilde{t} = 2.40$, 0.477, 0.240, 0.242, and 0.121, for shock waves A, B, C, D, and E, respectively.

4.1. *Parallel implementation*

The numerical problem of shock wave calculations considered here is very time consuming and requires a powerful computational system. We employed a cluster computer system consisting of up to 300 processors with distributed memory equipped either with Intel Pentium III, or with Alpha 21264 microprocessors. The Message Passing Interface (MPI) standard was used for the organization of interprocessor data exchange. The parallel code is geometrical-parallelism based, according to the domain decomposition technique. This means that the whole computational domain is divided into subdomains in the z-direction, with each processor providing the calculations in its own subdomain. The number of subdomains is equal to the number of processors used. Efficiency estimations show that the implemented numerical algorithm, explicit in time and homogeneous in space allows the efficient use of the cluster multiprocessor systems (Graur *et al.* 2002*a*).

4.2. *Flow and boundary conditions*

The QGD and QGDR numerical calculations were carried out under flow conditions suited for comparison with the experimental results. The nozzle exit quantities, some of which are required for the calculation, are reported in table 2. They have been obtained from the source conditions of the experiment assuming an isentropic approximation with $Ma_e = u_e/a_e = 1.01$ at the exit of the nozzle. The ratio of background to nozzle exit pressures of the five shock waves investigated are marked (A) to (E) in table 2.

A representative two-dimensional computational domain is shown in figure 1. The PQ, QR, RS, and SN, boundary conditions for the QGD and QGDR equations are as follows:

PQ (nozzle wall boundary)

$$u_z = 0, \quad \frac{\partial u_r}{\partial z} = 0, \quad \frac{\partial p}{\partial z} = 0, \quad \frac{\partial T}{\partial z} = 0, \tag{22}$$

QR (radial undisturbed boundary)

$$\frac{\partial u_z}{\partial r} = 0, \quad u_r = 0, \quad p = p_\infty, \quad T = T_\infty, \tag{23}$$

RS (downstream boundary)

$$\frac{\partial u_z}{\partial z} = 0, \quad \frac{\partial u_r}{\partial z} = 0, \quad \frac{\partial p}{\partial z} = 0, \quad \frac{\partial T}{\partial z} = 0, \tag{24}$$

SN (symmetry axis boundary)

$$\frac{\partial u_z}{\partial r} = 0, \quad u_r = 0, \quad \frac{\partial p}{\partial r} = 0, \quad \frac{\partial T}{\partial r} = 0. \tag{25}$$

4.3. *Schlieren pictures*

The global representation of the two-dimensional problem discussed next has been generated by means of a numerical schlieren picture. According to Liepmann & Roshko (1957) either $\partial\rho/\partial r$ or $\partial\rho/\partial z$ can be visualized in experimental schlieren pictures depending on the knife position, vertical or horizontal, respectively. For numerical visualization both possibilities can be used but, in accordance with our experience, the quantity best suited for a faithful picture is based on the absolute value of the gradient

$$|\nabla\rho| = \sqrt{\left(\frac{\partial\rho}{\partial z}\right)^2 + \left(\frac{\partial\rho}{\partial r}\right)^2}. \tag{26}$$

In order to expose even weak density non-uniformities, a nonlinear scale has been utilized as proposed by Quirk (1994, 1998). A schlieren picture corresponding to the flow field of expansion B is shown in figure 1. It depicts the quantity

$$S(z, r) = C \exp\left(-K \frac{|\nabla\rho| - |\nabla\rho|_{min}}{|\nabla\rho|_{max} - |\nabla\rho|_{min}}\right), \tag{27}$$

where the subscripts *min* and *max* denote the minimum and maximum values of the density gradient over the whole flow field; C and K are two tunable parameters. The parameter C determines the shade of grey that corresponds to the zero gradient, while K governs the amplification of small gradients. We have used $C = 0.8$, and K between 10 and 15.

5. Density, temperature, and velocity profiles of shock waves A, B, C, D, and E

The density, rotational temperature, and velocity, profiles of axisymmetric supersonic expansions and associated shock waves are characterized by a number of reference points, depicted schematically in figure 2 for a generic expansion. These points are located along the symmetry axis of the expansion.

Reference point 1, of abscissa z_1, in figure 2(*a*) corresponds to the minimum of density, n_1, in the zone of silence of the expansion. Point 2 corresponds to a

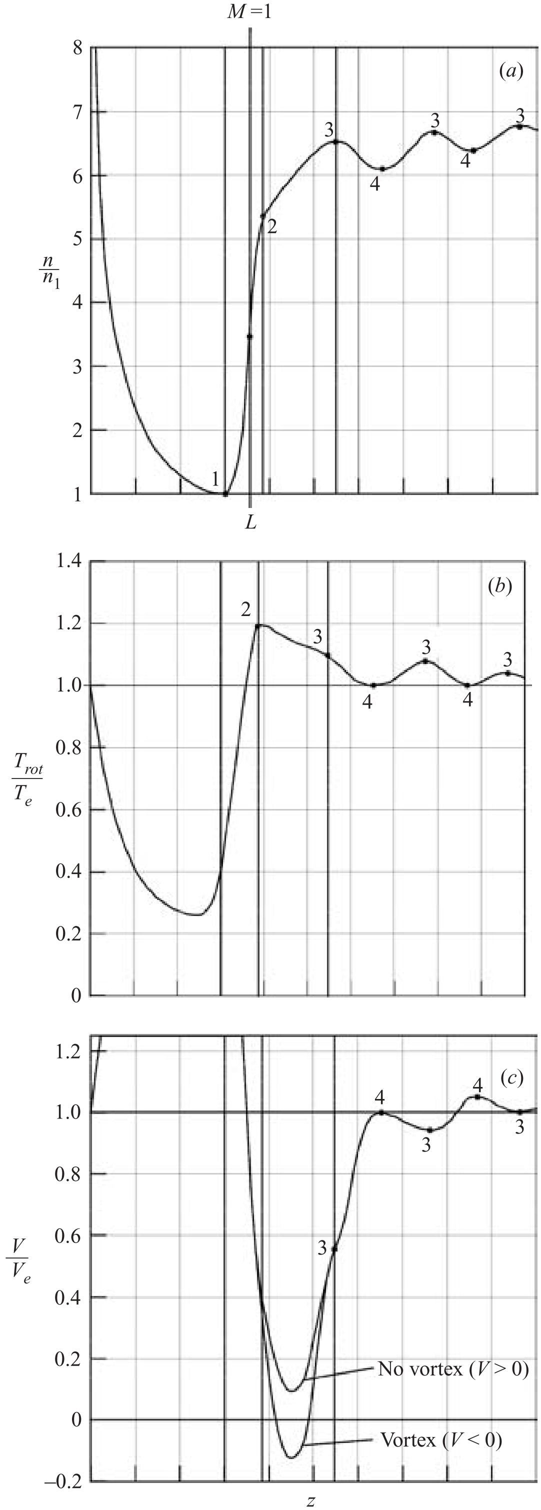

FIGURE 2. Reference points in a generic axisymmetric supersonic expansion; (*a*) densities, (*b*) rotational temperatures, and (*c*) velocities.

		A	B	C	D	E
z_1	QGDR	2.50	4.70	6.50	8.53	10.64
	Exptl	2.55	5.3	7.5	10.0	13.0
n_1	QGDR	21.46	4.84	2.27	1.18	0.70
	Exptl	30.6	6.3	3.3	1.8	0.93
L (Mach disk)	QGD[a]	2.58	4.93	7.75	9.16	13.79
	QGDR[a]	2.74	5.24	7.90	10.80	13.93
	Exptl[a]	2.7	6.1	8.5	11.6	15.25
z_{min}	Ashk.[b]	2.62	5.37	7.59	10.14	12.65
$\tilde{\lambda}^{max}$	QGDR	0.16	0.74	1.57	2.96	4.86
$z(\tilde{\lambda}^{max})$	QGDR	2.58	4.85	6.81	8.92	11.19
Kn^{max}	Exptl	0.33	0.35	0.42	0.54	0.59
$z(Kn^{max})$	Exptl	2.68	6.0	8.3	11.3	14.8
Kn^{max}	QGDR	0.62	0.87	1.06	1.40	1.79
$z(Kn^{max})$	QGDR	2.66	5.09	7.28	9.70	12.36

[a] from maximum density gradient, [b] from equation (28) according to Ashkenas & Sherman (1964), employing the effective nozzle radius $r_e^{eff} = 0.148$ mm.

Table 3. Numerical results on shock waves A, B, C, D, and E for computational variant $s2$, and comparison with experiment; z and L are distances downstream from the nozzle, in mm; n_1 is the minimum absolute number density on the axis, in units of 10^{21} m^{-3}; $\tilde{\lambda} = \lambda/(2r_e)$ is the normalized mean free path, and $Kn = (\lambda/n)(\mathrm{d}n/\mathrm{d}z)$ the local Knudsen number.

discontinuity in the slope of the density. To experimental accuracy, this discontinuity coincides with the highest rethermalization of the rotational temperature, about 20% above the nozzle exit temperature, T_e, as shown in figure 2(*b*). Along the expansion the first experimental evidence of the onset of the normal shock wave is the rethermalization, which starts upstream from point 1, of minimum density, shown in figure 2(*b*). This agrees with the predictions of Rebrov & Chekmarev (1971) for a spherically expanding flow, a good model for the paraxial region of the present expansions up to point 2. Point 2 may be considered the end of the actual shock wave.

Between points 1 and 2, the abscissa L of largest slope in the density profile of figure 2(*a*) coincides with the sonic condition $M = 1$. Customarily this point is referred to as the location of the Mach disk.

According to Ashkenas & Sherman (1964) the abscissa of minimum pressure upstream from the shock wave is given by

$$z_{min} = 1.34 r_e (p_0/p_\infty)^{1/2}, \tag{28}$$

where r_e is the radius of the nozzle, p_0 the stagnation pressure in the nozzle prechamber, and p_∞ the background pressure in the expansion chamber. The abscissa of point 1, z_1, its absolute number density, n_1, the location L of the Mach disk, and other relevant flow parameters of cases A to E are given in table 3, from the experiment, and computational variant $s2$. It should be noted that the abscissa of lowest pressure, z_{min}, from (28), is indeed very close to the experimental point 1 of lowest number density, but progressively departs from the true position of the Mach disk on going from shock A to shock E.

For all grids of table 1 QGDR results are somewhat closer to the experimental values. QGD results slightly underestimate the position of the Mach disk compared to QGDR results.

The density jump across the shock, between points 1 and 2 of figure 2(*a*), is found empirically to obey the relation

$$\frac{n_2}{n_1} = \left(\frac{z_1}{z_2}\right)^2 \frac{(\gamma+1)M^2}{2+(\gamma-1)M^2}, \tag{29}$$

where z_1 and z_2 are the axial distances from the nozzle to points 1, and 2, respectively, and M is the Mach number at the onset of the normal shock. The experimental values $M \approx 7.7$, 10.6, 12.2, 13.6, and 15.3, at the onset of shocks A, B, C, D, and E, respectively, have been estimated from the distance between the nozzle and the point of lowest rotational temperature according to the empirical parameterization of M as a function of z and γ proposed by Miller (1988). In the limit of infinitesimal width ($z_2 = z_1$), equation (29) leads to the Rankine–Hugoniot density jump across an ideal monodimensional shock wave. For increasingly larger widths of the real shock wave, i.e. for increasing mean free path, the discontinuity in the gradient of density at point 2 tends to vanish. In shock wave E it is no longer recognizable, but its location can be inferred approximately from the rethermalization of the rotational temperature.

Between points 2 and 3 the density gradient is positive, but smaller than at the shock, and at point 3 the density reaches a local maximum. Downstream from point 3 mild secondary expansions are observed, with a quasi-periodical structure of density maxima (points 3), and minima (points 4). As shown in figures 2(*a*) and 2(*b*), these density maxima and minima are correlated with temperature maxima and minima, but are anticorrelated with those of flow velocity (figure 2*c*).

The QGD and QGDR numerical simulation of these features shows an encouraging qualitative agreement with experiment for all five shock waves investigated. To what extent the simulation reaches a quantitative agreement very much depends on the grid employed, on the size of computational domain, on the sort of approximation, QGD versus QGDR, on the damping parameter β defined previously (equation (20)), and on the rarefaction at the onset of the shock. The influence of these factors is discussed next.

5.1. *Shock wave A*

The convergence of the QGD numerical solution with grid refinement is summarized in figure 3 for variants $s1$ to $s4$ (see table 1). Density profiles improve beyond point 2 for finer grids, as shown in figure 3(*a*), and in more detail in figure 4, calculated with the finest grid in a reduced computational domain. Altough variant $s8$ is still unable to reproduce the slope beyond point 2, the density jump between points 1 and 2 is predicted very accurately, as well as the slope between points 1 and 2. The Mach disk location L is not very sensitive to grid nor to domain size. For the variants of table 1 this position is in the range $2.504 \leqslant L \leqslant 2.676$ mm, on average 5% smaller than the experimental value $L(A) = 2.7$ mm.

Calculated temperature profiles shown in figure 3(*b*) slightly improve for finer grids only in the region of lowest temperatures prior to the shock wave. Otherwise, the calculated thermal profile of shock wave A is nearly insensitive to grid choice, at least at the spatial resolution of the present experiments. In general QGD calculations predict an average thermal profile which is in fairly good agreement with experiment, as shown in figure 3(*b*). In particular the thermal overshoot at point 2 is well reproduced. The sequence of maxima (points 3) and minima (points 4) for densities and temperatures shown in figure 3(*b*) is also well reproduced regardless of grid.

QGD calculated axial velocities are depicted in figure 3(*c*). A recirculation vortex characterized by negative axial velocities, located immediately downstream from

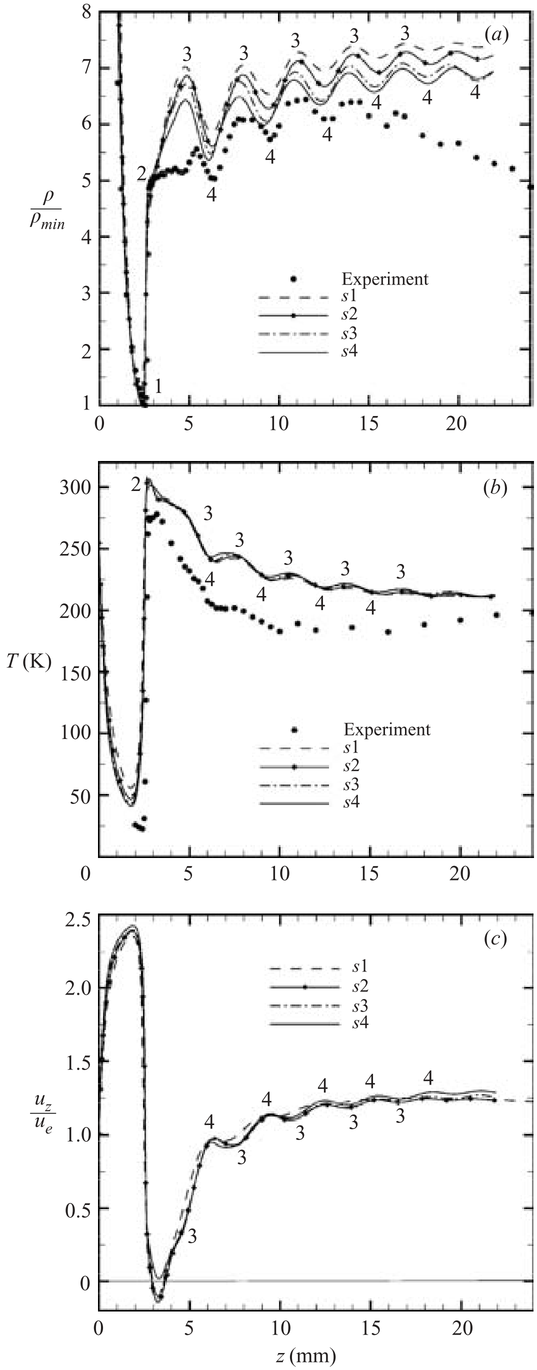

FIGURE 3. Shock wave A: experimental and QGD calculated axial profiles of density (*a*), temperature (*b*), and velocity (*c*), as a function of the grid; variants *s*1, *s*2, *s*3, and *s*4.

point 2, is obtained for *cv* grids in variants *s*1, *s*2, and *s*3, but not for the uniform finest grid in variant *s*4. Though the QGD description of the density profile between point 2 and the first point 3 is not good (gradient too large) it may be expected

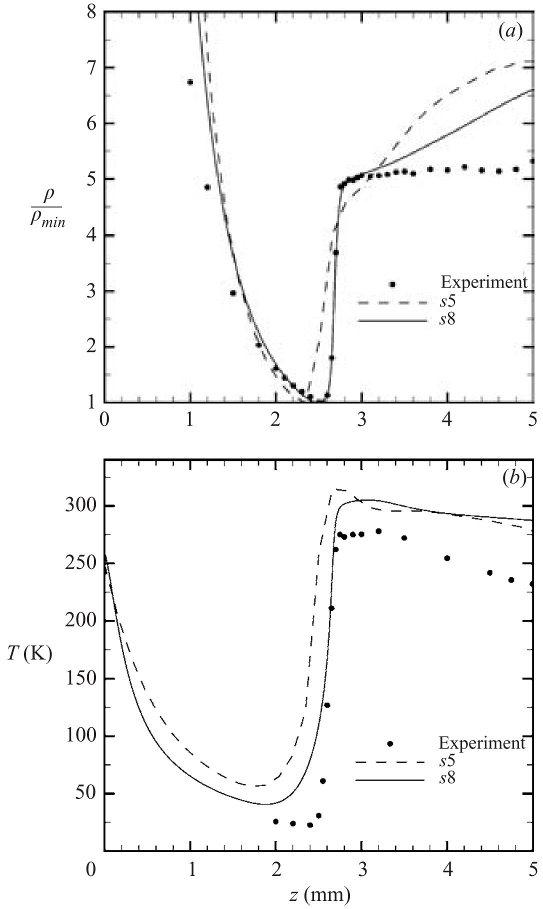

FIGURE 4. Shock wave A, detail: experimental and QGD calculated axial profiles of density (*a*), and temperature (*b*); variants $s5$ and $s8$.

that variant $s4$, yielding the closest gradient to the experiment, would also predict the velocity field best between 2 and 3. Indeed, in variant s4 the vortex disappears, suggesting that the vortex resulting in shock wave A for grids $s1$, $s2$, and $s3$, is a computational artifact with no physical reality.

The vortex also tends to vanish when the damping parameter is increased from $\beta = 0.1$ to 0.5, but this is probably caused by a smoothing of the calculated gradients of all quantities, including those of the velocity.

The differences between the QGD and the QGDR generalization are minor for shock wave A, as shown in figure 5 for variant $s2$. The QGDR prediction of Mach disk position, $L = 2.74$ mm, is closer to the experimental value $L = 2.7$ mm, but the sequence of maxima and minima, points 3 and 4, is not as good as for QGD calculation. As far as the presumed vortex is concerned, QGD and QGDR numerical results are similar.

5.2. *Shock wave B*

The convergence of QGD density profiles with grid refinement is shown in figure 6. In particular the density gradient around point 2 is well reproduced by variant $s3$. The thermal gradient is, however, less sensitive the to grid choice, as was the case

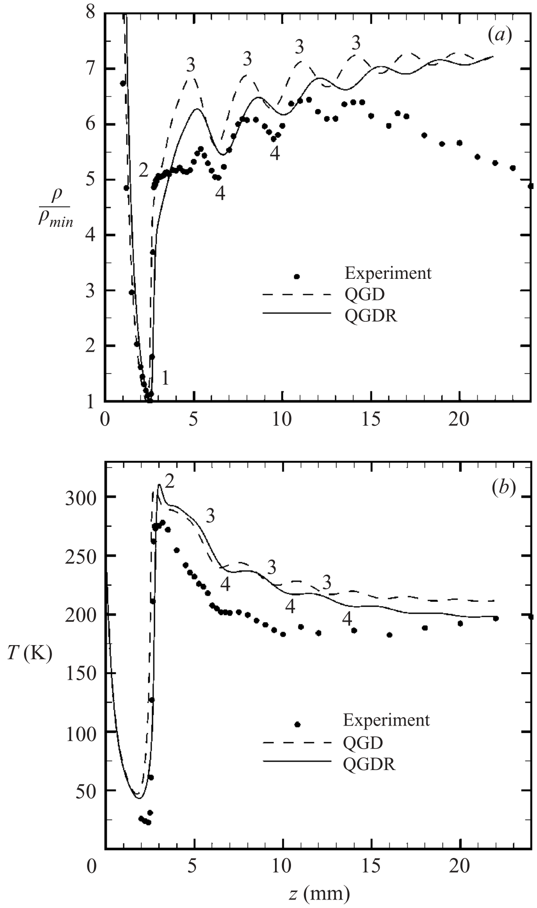

FIGURE 5. Shock wave A: QGD and QGDR calculated axial profiles of density (*a*), and rotational temperature (*b*); variant $s2$.

with shock wave A. Only a minor improvement is obtained with grid refinement. The position of the Mach disk is underestimated by about 20%, although the trend is towards an improvement with grid refinement. As was the case with shock wave A, shock wave B also displays a recirculation vortex for variants $s1$, $s2$, and $s3$.

The effect of using a uniform grid in a smaller computational domain, variant $s10$, is shown in figure 7. The density profile improves substantially between points 2 and 3, the region corresponding to the presumed vortex, but there is little change in the thermal profile. The pressure gradient appears be well reproduced by the calculation variant $s10$, so the small vortex in figure 7(*c*) between $z \approx 6$ and 7 mm, with reversed flow velocity $u_z \approx -0.1\ u_{ze}$ is obtained as a persistent numerical solution.

The QGDR generalization, even at the computational level of the coarse grid of variant $s2$, yields a substantial improvement compared to QGD density and temperature profiles, as shown in figure 8. The position of the Mach disk improves, and QGDR density maxima and minima, points 3 and 4, are very well reproduced, as are rotational temperatures above 150 K. The thermal onset of the shock wave, below 100 K, is, however, poorly reproduced by any computational variant. The initial section of the calculated thermal profile at the shock wave is far smoother than the

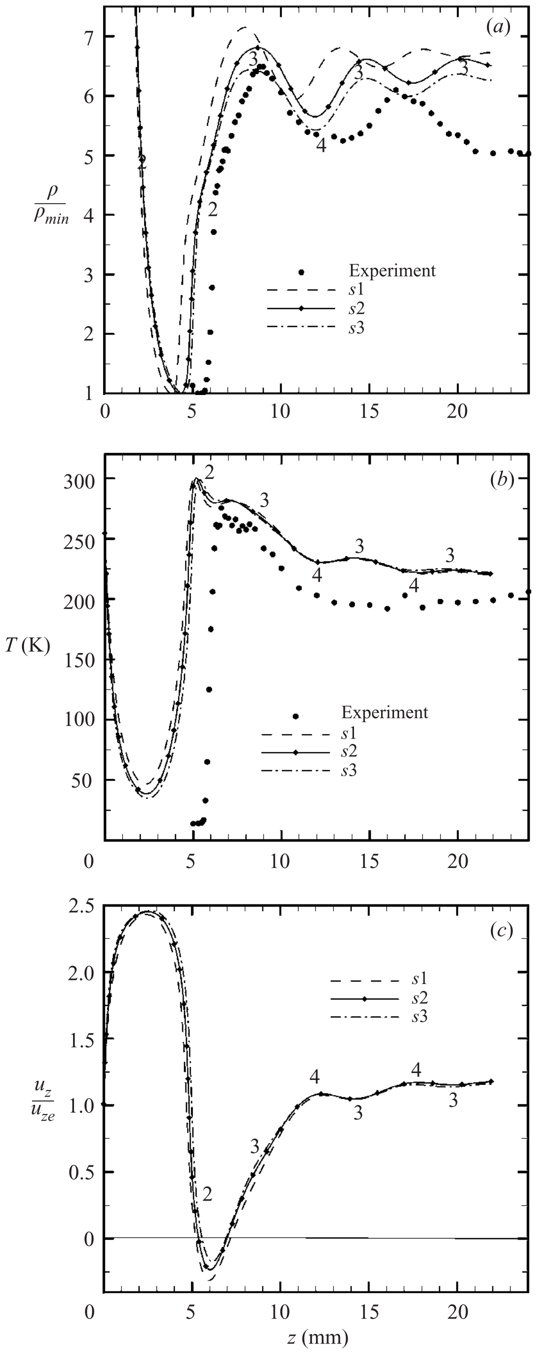

FIGURE 6. Shock wave B: experimental and QGD calculated axial profiles of density (*a*), temperature (*b*), and velocity (*c*), as a function of the grid; variants $s1$, $s2$, and $s3$.

experimental one. This mismatch is already evident in shock wave A, and worsens considerably the more rarefied is the flow at the point 1 of the shock wave. QGDR and QGD numerical behaviours of the vortex are similar.

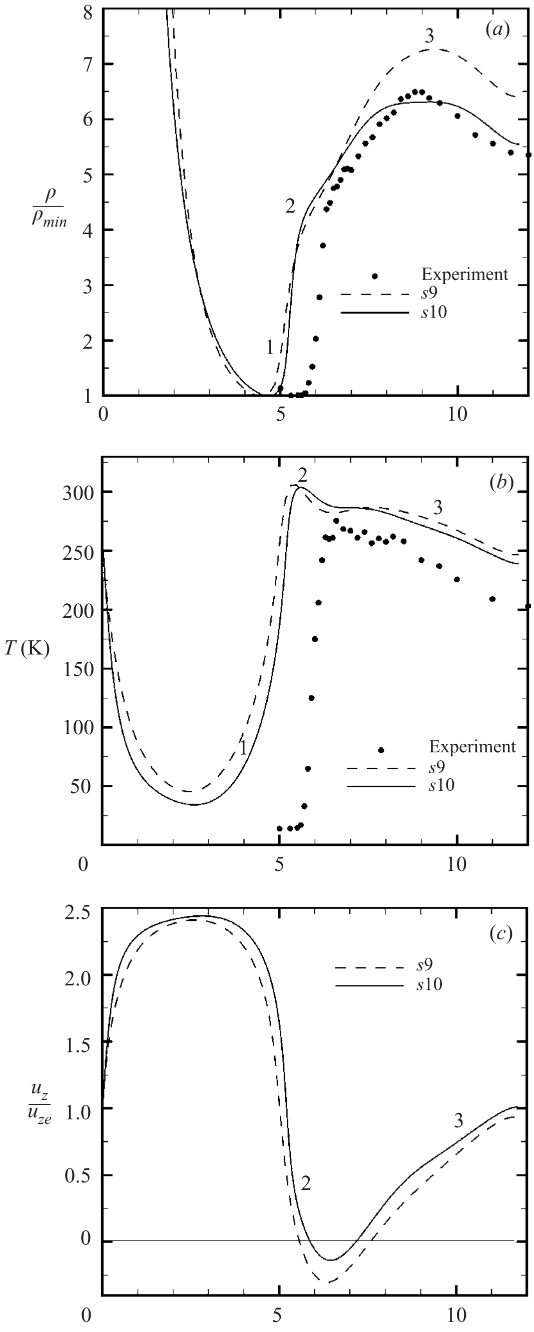

FIGURE 7. Shock wave B, detail: QGD calculated axial profiles of density (*a*), temperature (*b*), and velocity (*c*); variants *s*9 and *s*10.

5.3. *Shock waves C, D, and E*

Numerical and experimental results concerning shock waves C, D, and E, are depicted in figures 9 to 13. For these shock waves, with $Re_L < 100$, the influence of the grid on

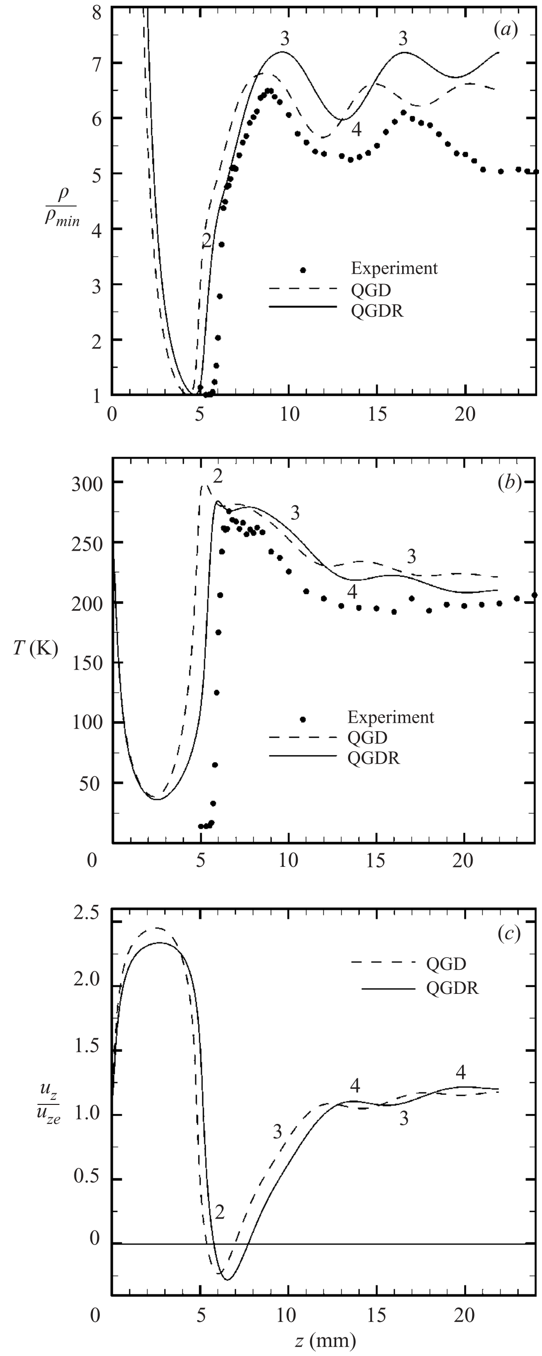

FIGURE 8. Shock wave B: QGD and QGDR calculated axial profiles of density (*a*), rotational temperature (*b*), and velocity (*c*); variant *s*2.

the QGD numerical results is of decreasing importance, as can be seen from figure 9 (shock wave C), and figure 11 (shock wave D). This is not surprising since the density and temperature gradients tend to be smoother the lower the density at the onset of the shock wave.

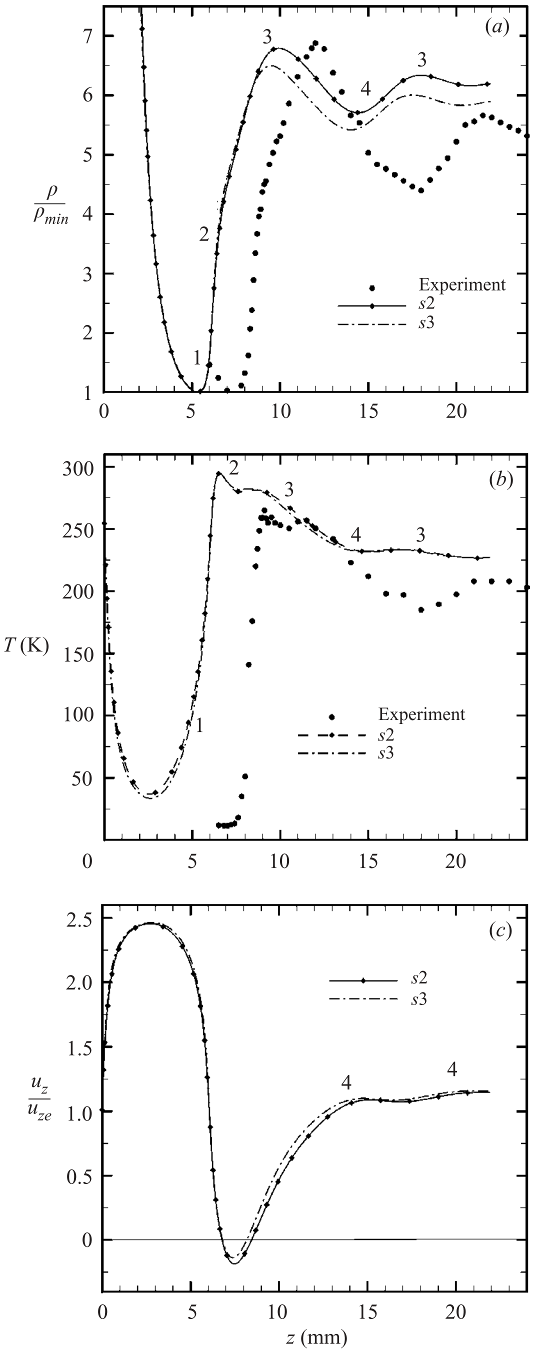

FIGURE 9. Shock wave C: QGD calculated axial profiles of density (*a*), temperature (*b*), and velocity (*c*), as a function of the grid; variants *s*2 and *s*3.

QGDR profiles are substantially closer to experiment than QGD profiles as shown in figure 10 (shock wave C), figure 12 (shock wave D), and figure 13 (shock wave E). This proves the superiority of QGDR over the plain QGD approach in these systems,

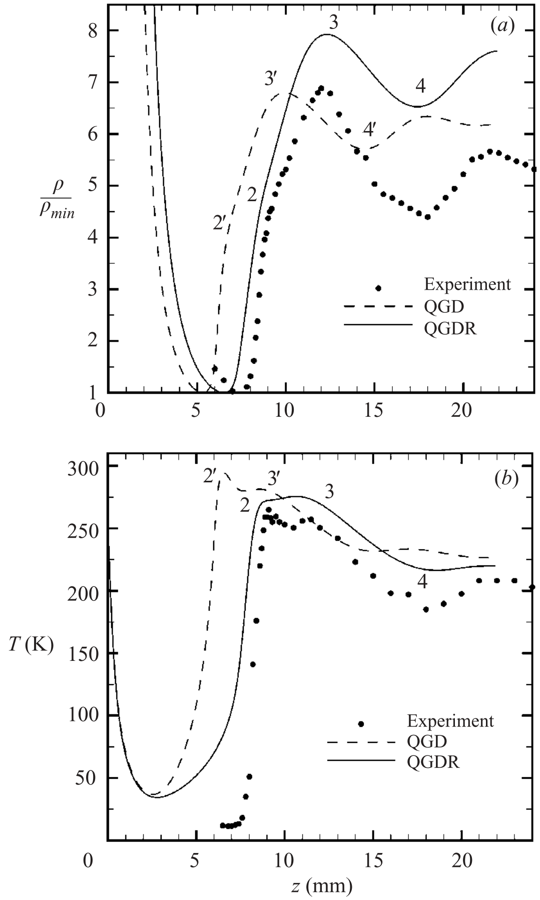

FIGURE 10. Shock wave C: QGD (primed numbers) and QGDR calculated axial profiles of density (*a*), and rotational temperature (*b*); variant *s*2.

or regions, of the flow field where rotational–translational relaxation effects are far from neglegible.

The numerical recirculation vortex appears for variants *s*2 and *s*3 in shocks C and D, but for shock D it disappears for variant *s*10. For shock E no vortex is detectable in the calculated flow field of velocities, but is obtained for the mass flux vector field J^i.

6. Discussion

The absolute number density along expansions A to E varies from $n_e = 1.1 \times 10^{25}$ m^{-3}, at the nozzle exit, up to a minimum value n_1 at point 1, three to four orders of magnitude smaller than n_e. A remarkable merit of the QGDR approach is its capability of accounting for this wide range of absolute number densities with fractional deviation

$$\Delta = \frac{\left| n_1^{QGDR} - n_1^{exptl} \right|}{n_e - n_1}, \tag{30}$$

well below 10^{-3} for all five expansions, according to the values given in table 3. In figures 3 to 13 it is shown how the normalized density profiles of shock waves A to

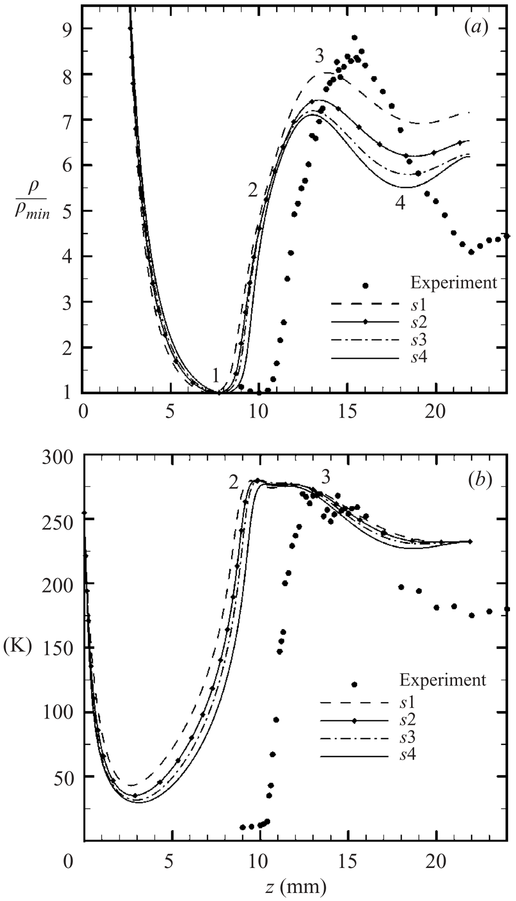

FIGURE 11. Shock wave D: experimental and QGD calculated axial profiles of density (*a*), and temperature (*b*), as a function of the grid; variants *s*1, *s*2, *s*3, and *s*4.

E are reproduced by the various computational variants described in the previous sections.

The systems studied here are associated with increasingly rarefied flows where the maximum value, Kn^{max}, of the local Knudsen number defined in the caption of table 3, is reached in the initial section of the shock wave; Kn^{max} progresively increases from shock wave A to shock wave E, as shown in table 3. These high values of Kn^{max} are due to the large mean free path λ at the onset of the shock wave (λ, inversely proportional to the number density, increases here by three to four orders of magnitude from nozzle to shock wave), divided by a small density, and multiplied by the large density gradient within the shock wave. This large variation of local Knudsen number between nozzle and shock wave, together with its intrinsic high value inside the shock wave, suggests that the present problem is in the limit of applicability of continuum models like QGD and QGDR.

It may be argued however whether the poor description of the QGDR rotational temperature profiles in the low-temperature section prior to the softer shock waves (see figures 10*b*, 12*b*, and 13*b*) is caused by an inaccurate estimate of the viscosity for $T < 100$ K. In order to check this point shock wave E, exhibiting the largest local Knudsen number, has been recalculated in the QGDR approach using a

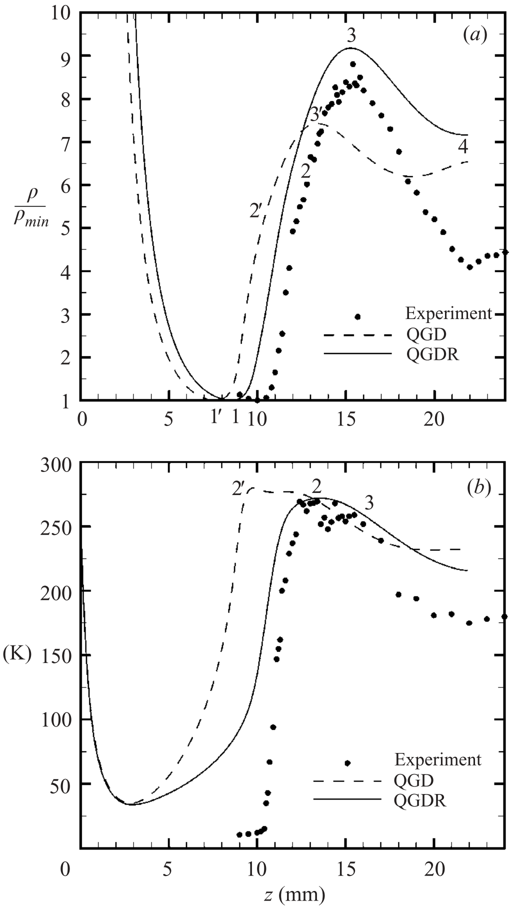

FIGURE 12. Shock wave D: QGD and QGDR calculated axial profiles of density (*a*), and rotational temperature (*b*); variant *s*2.

Sutherland-type viscosity law (Hirschfelder, Curtiss & Bird 1954) for nitrogen, where

$$\mu = 1.374 \times 10^{-6} \frac{T^{3/2}}{T + 100} \quad \text{for} \quad T > 100\,\text{K}, \tag{31}$$

$$\mu = 1.374 \times 10^{-6} \frac{T}{2\sqrt{100}} \quad \text{for} \quad T < 100\,\text{K}. \tag{32}$$

This viscosity law does indeed improve the lowest value of the rotational temperature in case E by ≈30%, but does not improve significantly the too smooth nature of the thermal onset of the shock wave. So we conclude that the too smooth calculated thermal gradient at the onset of the shock waves is an intrinsic limitation of the models based in the hypothesis of a continuum.

This limitation may be aggravated under conditions of severe breakdown of rotational–translational equilibrium, as is the case within the present shock waves. This is an unavoidable limitation of the QGD and QGDR models, and in general of continuum models, where the rotational distribution function is based on the hypothesis of continuous rotational energy, ignoring the discrete nature of rotational quantum levels. The very low temperatures at the beginning of the present shock waves preclude any reasonable averaging of the rotational distribution function.

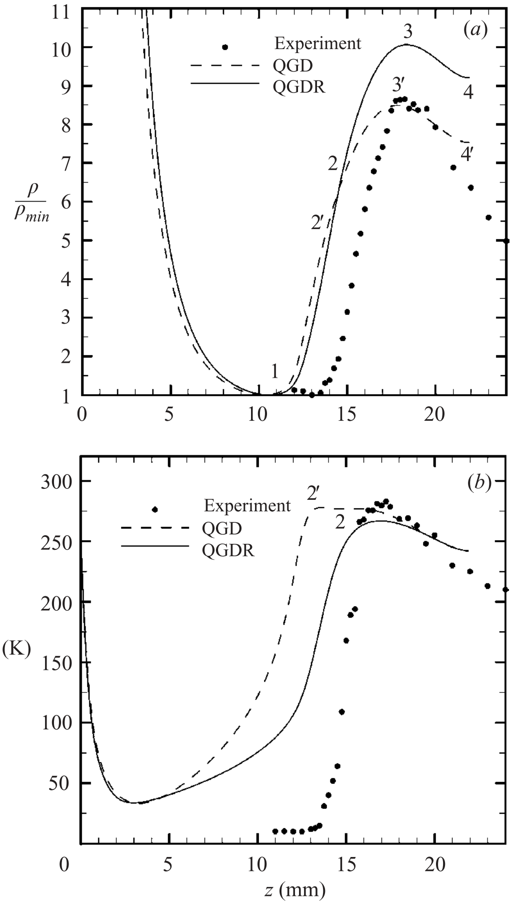

FIGURE 13. Shock wave E: experimental, QGD and QGDR calculated axial profiles of density (*a*), and rotational temperature (*b*); variant *s*2.

The above problems may in part be overcome by the direct simulation Monte Carlo method (DSMC). But in the particular problem treated here it brings additional computational difficulties due to the large differences of geometrical features in cases A to E, with very strong density and pressure gradients in the flow. This has been shown by Teshima & Usami (2001), who had to employ different size cells and different time-step schemes to treat a similar problem.

In spite of the specific discrepancies mentioned above the, overall agreement between numerical and experimental profiles of density and rotational temperature confer on the present results, specially the QGDR ones, a reasonable degree of credibility. A striking feature of the calculated flow fields is the steady recirculation vortex, trapped immediately downstream from the shock wave, which appears as a stable numerical solution when using coarse grids (Graur *et al.* 2002*b*). These sorts of solutions are summarized in figure 14 showing an overview of the velocity field. There the nature of reference point 2 can be related to sudden changes in the orientation of the velocity vector. Similar vortices have been described before in the literature, but no experimental proof of their physical reality has been reported, as far as we are aware. In the light of the present experimental and numerical results it is not possible to confirm, or to deny, whether they are spurious numerical solutions or not.

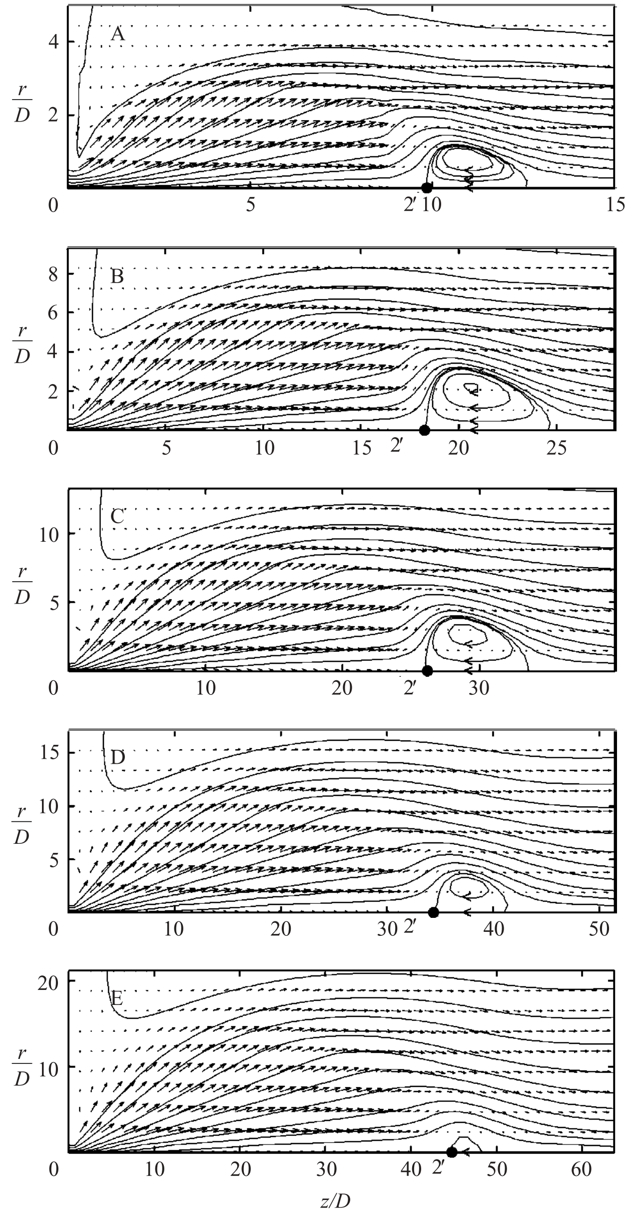

FIGURE 14. QGDR flow fields of N_2 expansions A, B, C, D, and E, calculated with variant $s2$; $2'$ indicates the calculated position of reference point 2; $D = 2r_e$ is the nozzle diameter.

In the experiment, the very slow velocity beyond the shock wave, with or without recirculation, is too low to be detectable with the spectroscopic technique employed. The present numerical solutions indicate, however, the tendency of the vortex to vanish, in most cases but not always, when finer computational grids are used. Even with the finest grid compatible with our computational hardware resources, the vortex of shock wave B remains as a stable numerical solution. Only a substantial increase of these resources can in principle remove this ambiguity by employing still finer grids. In any case it is worth noticing the extreme computational sensibility of the velocity flow field that can be inferred from figure 14 in the vortex region. There the orientation and magnitude of the velocity vector appears as an extremely sensitive test for gasdynamical models and computational variants. Note however that the present approach is restricted by r–z geometry, but the actual flow might be fully three-dimensional, a possibility that should not be excluded *a priori*. The recirculation flow behind the Mach disk might indeed be more complicated than a simple stationary vortex with axial symmetry. Since in the present problem $Re_e \approx 3200$, at the nozzle exit the flow might be spiraliform, or might even have a more complicated topology, as is known to happen in flows behind obstacles, even for rather small Re (Shevelev 1986; Perry & Chong 1987; Mason & Sykes 1979; Shevelev & Klekovkin 2003).

7. Conclusions

The present work shows to what extent a gasdynamic problem with a wide range of local Knudsen numbers can be treated within the framework of the QGD/QGDR approach. The following conclusions can be drawn:

(i) The QGD equations, and specially their QGDR generalization, provide a reasonable description of axial densities, and a somewhat less accurate description of temperatures, in two-dimensional flow fields of supersonically expanding N_2, with measured local Knudsen number up to $Kn < 0.6$, approximately. These flow fields include normal shock waves in the range of Mach numbers $7.7 < M < 15.3$.

(ii) The less satisfactory feature of the QGD approach is the description of the thermal evolution at the onset of the shock waves, the most rarefied region of the flow field. This numerical description of temperatures is moderately good in regions with experimental local Knudsen number $Kn \leqslant 0.3$. However, wherever $Kn \approx 0.6$ it worsens considerably. The QGDR generalization overcomes in part this limitation but still predicts a too smooth profile for the rotational temperature at the onset of the shock waves. Since the translational distribution function is free from quantum effects, the translational temperatures may be expected to be better described by the QGDR approach than the rotational temperatures, specially at the lower end of the thermal scale. Unfortunately, this conjecture cannot be proved from the present experiment since translational temperature is not amenable to direct measure.

(iii) The gradients of the gasdynamic quantities decrease markedly with increasing rarefaction and mean free path, on going from shock wave A to shock wave E. The larger the mean free path, as in shock wave E, the less determinant is the choice of computational grid. On the other hand, shock wave A is particularly sensitive to the density and type of computational grid.

(iv) Parallel implementation of the QGD and QGDR equations in this problem has proved highly advantageous.

(v) The physical reality of the recirculation vortex formed immediately downstream from the shock wave associated with axisymmetric hypersonic expansions cannot be proved unambiguously from the present experimental data, nor from the QGD or QGDR numerical results. In some cases the numerical vortex disappears when dense enough grids are employed in the calculation. The vortex must so far remain conjectural in our opinion.

(vi) Linear Raman spectroscopy proves to be an instrumental technique very well suited for the quantitative study of normal shock waves. For shock waves spanning a wide range of their gasdynamic quantities it can provide

(*a*) sampling at very high spatial resolution (few µm)
(*b*) absolute densities (±10%) within several orders of magnitude
(*c*) rotational temperatures (±5%) nearly unlimited in range.

This work was supported by the Russian Foundation for Basic Research, grant N 01-01-00061, and by the Spanish DGESIC (MEC), research project PB97-1203. Thanks are due to the referees for the valuable comments towards the improvement of this paper.

Appendix A. The r, z-formulation

The present QGD and QGDR equations in the r, z formulation differ from the version given by Maté *et al.* (2001). The NS dissipative terms, and the additional dissipative terms, are written here separately. For brevity we just report the r, z-formulation for the QGD system. In the case of r, z geometry equations (1)–(3) take the form

$$\frac{\partial \rho}{\partial t} + \frac{1}{r}\frac{\partial}{\partial r}(r J^r) + \frac{\partial}{\partial z} J^z = 0, \tag{A 1}$$

$$\frac{\partial(\rho u_r)}{\partial t} + \frac{1}{r}\frac{\partial}{\partial r}(r J^r u_r) + \frac{\partial}{\partial z}(J^z u_r) + \frac{\partial p}{\partial r} = \frac{1}{r}\frac{\partial}{\partial r}(r \Pi^{rr}) + \frac{\partial}{\partial z}\Pi^{zr} - \frac{\Pi^{\varphi\varphi}}{r}, \tag{A 2}$$

$$\frac{\partial(\rho u_z)}{\partial t} + \frac{1}{r}\frac{\partial}{\partial r}(r J^r u_z) + \frac{\partial}{\partial z}(J^z u_z + p) = \frac{1}{r}\frac{\partial}{\partial r}(r \Pi^{rz}) + \frac{\partial}{\partial z}\Pi^{zz}, \tag{A 3}$$

$$\begin{aligned}\frac{\partial E}{\partial t} + \frac{1}{r}\frac{\partial}{\partial r} r J^r \frac{(E+p)}{\rho} + \frac{\partial}{\partial z} J^z \frac{(E+p)}{\rho} + \frac{1}{r}\frac{\partial}{\partial r}(r q^r) + \frac{\partial}{\partial z} q^z \\ = \frac{1}{r}\frac{\partial}{\partial r} r(\Pi^{rr} u_r + \Pi^{rz} u_z) + \frac{\partial}{\partial z}(\Pi^{zr} u_r + \Pi^{zz} u_z),\end{aligned} \tag{A 4}$$

where

$$E = \rho\frac{u_r^2 + u_z^2}{2} + \frac{p}{\gamma - 1}.$$

The expressions for the mass flux vector, the heat flux vector, and the shear stress tensor are:

$$\left.\begin{aligned} J_{NS}^r = \rho u_r, \qquad J_D^r &= -\tau\left(\frac{1}{r}\frac{\partial}{\partial r}(r\rho u_r^2) + \frac{\partial p}{\partial r} + \frac{\partial}{\partial z}(\rho u_r u_z)\right), \\ J_{NS}^z = \rho u_z, \qquad J_D^z &= -\tau\left(\frac{1}{r}\frac{\partial}{\partial r}(r\rho u_r u_z) + \frac{\partial}{\partial z}(\rho u_z^2) + \frac{\partial p}{\partial z}\right), \end{aligned}\right\} \tag{A 5}$$

$$\left.\begin{aligned} q_{NS}^r &= -\frac{\gamma}{\gamma-1}\frac{1}{Pr}\frac{\partial}{\partial r}\left(\frac{p}{\rho}\right), \qquad q_{NS}^z = -\frac{\gamma}{\gamma-1}\frac{1}{Pr}\frac{\partial}{\partial z}\left(\frac{p}{\rho}\right), \\ q_D^r &= -\tau\left(\frac{\rho u_r}{\gamma-1}\left(u_r\frac{\partial}{\partial r}\left(\frac{p}{\rho}\right) + u_z\frac{\partial}{\partial z}\left(\frac{p}{\rho}\right)\right) + \rho u_r p\left(u_r\frac{\partial}{\partial r}\left(\frac{1}{\rho}\right) + u_z\frac{\partial}{\partial z}\left(\frac{1}{\rho}\right)\right)\right), \\ q_D^z &= -\tau\left(\frac{\rho u_z}{\gamma-1}\left(u_r\frac{\partial}{\partial r}\left(\frac{p}{\rho}\right) + u_z\frac{\partial}{\partial z}\left(\frac{p}{\rho}\right)\right) + \rho u_z p\left(u_r\frac{\partial}{\partial r}\left(\frac{1}{\rho}\right) + u_z\frac{\partial}{\partial z}\left(\frac{1}{\rho}\right)\right)\right), \end{aligned}\right\} \tag{A 6}$$

$$\left.\begin{aligned}
\Pi_{NS}^{rr} &= 2\mu\frac{\partial u_r}{\partial r} - (\gamma - 1)\mu\nabla\cdot\boldsymbol{u},\\
\Pi_{NS}^{zr} &= \Pi_{NS}^{rz} = \mu\left(\frac{\partial u_r}{\partial z} + \frac{\partial u_z}{\partial r}\right),\\
\Pi_{NS}^{zz} &= 2\mu\frac{\partial u_z}{\partial z} - (\gamma - 1)\mu\nabla\cdot\boldsymbol{u},\\
\Pi_{NS}^{\varphi\varphi} &= 2\mu\frac{u_r}{r} - (\gamma - 1)\mu\nabla\cdot\boldsymbol{u}.
\end{aligned}\right\} \tag{A 7}$$

$$\left.\begin{aligned}
\Pi_{D}^{rr} &= \tau\left(\rho u_r^2\frac{\partial u_r}{\partial r} + \rho u_r u_z\frac{\partial u_r}{\partial z} + 2u_r\frac{\partial p}{\partial r} + u_z\frac{\partial p}{\partial z} + \gamma p\nabla\cdot\boldsymbol{u}\right),\\
\Pi_{D}^{rz} &= \tau\left(\rho u_r^2\frac{\partial u_z}{\partial r} + \rho u_r u_z\frac{\partial u_z}{\partial z} + u_r\frac{\partial p}{\partial z}\right),\\
\Pi_{D}^{zr} &= \tau\left(\rho u_r u_z\frac{\partial u_r}{\partial r} + \rho u_z^2\frac{\partial u_r}{\partial z} + u_z\frac{\partial p}{\partial r}\right),\\
\Pi_{D}^{zz} &= \tau\left(\rho u_r u_z\frac{\partial u_z}{\partial r} + \rho u_z^2\frac{\partial u_z}{\partial z} + 2u_z\frac{\partial p}{\partial z} + u_r\frac{\partial p}{\partial r} + \gamma p\nabla\cdot\boldsymbol{u}\right),\\
\Pi_{D}^{\varphi\varphi} &= \tau\left(u_r\frac{\partial p}{\partial r} + u_z\frac{\partial p}{\partial z} + \gamma p\nabla\cdot\boldsymbol{u}\right),
\end{aligned}\right\} \tag{A 8}$$

$$\nabla\cdot\boldsymbol{u} = \frac{1}{r}\frac{\partial(ru_r)}{\partial r} + \frac{\partial u_z}{\partial z}.$$

It should be mentioned that in the r, z formulation the flow quantities are uniform on azimutal angle φ, with vanishing derivatives on it. However, the stress tensor component $\Pi^{\varphi\varphi}$ is independent of φ, and is non-zero even in the r, z formulation.

Appendix B. Numerical realization

For the numerical realization the system (A 1) – (A 4) is rewritten in the vector-form:

$$\begin{aligned}
&\frac{\partial \boldsymbol{U}}{\partial t} + \frac{1}{r}\frac{\partial(r\boldsymbol{F})}{\partial r} + \frac{\partial \boldsymbol{F}_1}{\partial r} + \frac{1}{r}\frac{\partial(r\boldsymbol{F}_D)}{\partial r} + \frac{\partial \boldsymbol{E}}{\partial z} + \frac{\partial \boldsymbol{E}_D}{\partial z}\\
&\qquad = \frac{1}{r}\frac{\partial(r\boldsymbol{W})}{\partial r} + \frac{1}{r}\frac{\partial(r\boldsymbol{W}_D)}{\partial r} + \frac{\partial \boldsymbol{V}}{\partial z} + \frac{\partial \boldsymbol{V}_D}{\partial z} - \frac{\boldsymbol{G}}{r} - \frac{\boldsymbol{G}_D}{r},
\end{aligned} \tag{B 1}$$

where

$$\boldsymbol{U} = \begin{pmatrix}\rho\\ \rho u_r\\ \rho u_z\\ E\end{pmatrix},\quad \boldsymbol{F} = \begin{pmatrix}J_{NS}^r\\ u_r J_{NS}^r\\ u_z J_{NS}^r\\ J_{NS}^r(E+p)/\rho\end{pmatrix},\quad \boldsymbol{E} = \begin{pmatrix}J_{NS}^z\\ u_r J_{NS}^z\\ u_z J_{NS}^z + p\\ J_{NS}^z(E+p)/\rho\end{pmatrix},\quad \boldsymbol{F}_1 = \begin{pmatrix}0\\ p\\ 0\\ 0\end{pmatrix}, \tag{B 2}$$

$$\boldsymbol{F}_D = \begin{pmatrix}J_D^r\\ u_r J_D^r\\ u_z J_D^r\\ J_D^r(E+p)/\rho\end{pmatrix},\quad \boldsymbol{E}_D = \begin{pmatrix}J_D^z\\ u_r J_D^z\\ u_z J_D^z\\ J_D^z(E+p)/\rho\end{pmatrix},\quad \boldsymbol{G} = \begin{pmatrix}0\\ \Pi_{NS}^{\varphi\varphi}\\ 0\\ 0\end{pmatrix},\quad \boldsymbol{G}_D = \begin{pmatrix}0\\ \Pi_{D}^{\varphi\varphi}\\ 0\\ 0\end{pmatrix}, \tag{B 3}$$

$$\boldsymbol{W}=\begin{pmatrix} 0 \\ \Pi_{NS}^{rr} \\ \Pi_{NS}^{rz} \\ u_r\Pi_{NS}^{rr}+u_z\Pi_{NS}^{rz}-q_{NS}^{r} \end{pmatrix}, \qquad \boldsymbol{W}_D=\begin{pmatrix} 0 \\ \Pi_{D}^{rr} \\ \Pi_{D}^{rz} \\ u_r\Pi_{D}^{rr}+u_z\Pi_{D}^{rz}-q_{D}^{r} \end{pmatrix}, \tag{B 4}$$

$$\boldsymbol{V}=\begin{pmatrix} 0 \\ \Pi_{NS}^{zr} \\ \Pi_{NS}^{zz} \\ u_r\Pi_{NS}^{zr}+u_z\Pi_{NS}^{zz}-q_{NS}^{z} \end{pmatrix}, \qquad \boldsymbol{V}_D=\begin{pmatrix} 0 \\ \Pi_{D}^{zr} \\ \Pi_{D}^{zz} \\ u_r\Pi_{D}^{zr}+u_z\Pi_{D}^{zz}-q_{D}^{z} \end{pmatrix}. \tag{B 5}$$

As mentioned in § 4, in order to stabilize the numerical algorithm the relaxation time τ is replaced by $\tau+\tau_{eff}$ in several dissipative terms of the QGD and QGDR systems. In particular, in the QGD system this procedure is employed for the $\boldsymbol{J}_D$ and $\boldsymbol{q}_D$ vectors, and for the $\boldsymbol{\Pi}_D$ and $\boldsymbol{\Pi}_{NS}$ tensors as follows: the replacement is made only in the terms of the system (A 1) – (A 4) obtained by taking the derivatives of $\boldsymbol{J}_D$, $\boldsymbol{q}_D$, $\boldsymbol{\Pi}_D$, and $\boldsymbol{\Pi}_{NS}$, that would include second derivatives in the r and z coordinates. The corresponding terms for the $\boldsymbol{J}_D$ and $\boldsymbol{q}_D$ vectors, and for the $\boldsymbol{\Pi}_D$ tensor, are

$$\frac{\partial}{\partial z}(\tau+\tau_{eff})\frac{\partial f}{\partial z}, \quad \frac{\partial}{\partial z}(\tau+\tau_{eff})g\frac{\partial g}{\partial z},$$

$$\frac{1}{r}\frac{\partial}{\partial r}(\tau+\tau_{eff})\frac{\partial}{\partial r}(rf), \quad \frac{1}{r}\frac{\partial}{\partial r}(\tau+\tau_{eff})g\frac{\partial}{\partial r}(rg), \quad \frac{1}{r}\frac{\partial}{\partial r}(\tau+\tau_{eff})rg\frac{\partial g}{\partial r},$$

$$\frac{\partial}{\partial r}r(\tau+\tau_{eff})\frac{\partial g}{\partial r}, \quad \frac{1}{r}(\tau+\tau_{eff})g\frac{\partial g}{\partial r}, \quad \frac{1}{r^2}(\tau+\tau_{eff})g\frac{\partial}{\partial r}(rg),$$

where f and g are the functions of the gasdynamic parameters $f=f(\rho,u_r,u_z,p,E)$, and $g=g(u_r,u_z,p)$. For the $\boldsymbol{\Pi}_{NS}$ tensor the corresponding terms are

$$\frac{\partial}{\partial z}(\mu+\tau_{eff}p)\frac{\partial f}{\partial z}, \quad \frac{\partial}{\partial z}(\mu+\tau_{eff}p)g\frac{\partial g}{\partial z},$$

$$\frac{1}{r}\frac{\partial}{\partial r}(\mu+\tau_{eff}p)g\frac{\partial}{\partial r}(rg), \quad \frac{1}{r}\frac{\partial}{\partial r}(\mu+\tau_{eff}p)rg\frac{\partial g}{\partial r}.$$

The terms proportional to τ_{eff} are combined together in the vector form

$$\boldsymbol{FW}_{\tau_{eff}}=r\begin{pmatrix} -J_D^r \\ -u_rJ_D^r+\Pi_D^{rr}+\Pi_{NS}^{rr} \\ -u_zJ_D^r+\Pi_D^{rz} \\ -J_D^r(E+p)/\rho+u_r\Pi_D^{rr}+u_z\Pi_D^{rz}-q_D^r+u_r\Pi_{NS}^{rr} \end{pmatrix}, \tag{B 6}$$

$$\boldsymbol{EV}_{\tau_{eff}}=\begin{pmatrix} -J_D^z \\ -u_rJ_D^z+\Pi_D^{zr} \\ -u_zJ_D^z+\Pi_D^{zz}+\Pi_{NS}^{zz} \\ -J_D^z(E+p)/\rho+u_r\Pi_D^{zr}+u_z\Pi_D^{zz}-q_D^z+u_z\Pi_{NS}^{zz} \end{pmatrix}, \tag{B 7}$$

$$\boldsymbol{GG}_{\tau_{eff}} = \begin{pmatrix} 0 \\ \Pi_D^{\varphi\varphi} + \Pi_{NS}^{\varphi\varphi} \\ 0 \\ 0 \end{pmatrix}, \tag{B 8}$$

and finally the system (B 1) is rewritten in the form

$$\frac{\partial \boldsymbol{U}}{\partial t} + \frac{1}{r}\frac{\partial (r\boldsymbol{F})}{\partial r} + \frac{\partial \boldsymbol{F}_1}{\partial r} + \frac{\partial \boldsymbol{E}}{\partial z} = \frac{1}{r}\frac{\partial (r\boldsymbol{W})}{\partial r} + \frac{\partial \boldsymbol{V}}{\partial z} - \frac{\boldsymbol{G}}{r} + \frac{1}{r}\frac{\partial}{\partial r} r(-\boldsymbol{F}_D + \boldsymbol{W}_D)$$
$$+ \frac{\partial}{\partial z}(-\boldsymbol{E}_D + \boldsymbol{V}_D) - \frac{\boldsymbol{G}_D}{r} + \frac{1}{r}\frac{\partial (r\boldsymbol{W}\boldsymbol{F}_{\tau_{eff}})}{\partial r} + \frac{\partial (\boldsymbol{V}\boldsymbol{E}_{\tau_{eff}})}{\partial z} - \frac{\boldsymbol{GG}_{\tau_{eff}}}{r}. \tag{B 9}$$

The implementation of the ‘effective’ relaxation time τ_{eff} for the stabilization of numerical solution is analogous to the QGD-vector-splitting method developed and studied by Graur (2001), and used for the solution of the QGD equations.

REFERENCES

Ashkenas, H. & Sherman, F. S. 1964 The structure and utilization of supersonic free jets in low density wind tunnels. In *Proc. 4th Intl Symp. Rarefied Gas Dynamics* (ed. J. H. de Leeuw), vol. 2, pp. 84–105. Academic.

Benedict, R. P. 1966 Most probable discharge coefficient for ASME flow nozzles. *Trans. ASME: J. Basic Engng* 734.

Bird, G. A. 1994 *Molecular Gas Dynamics and the Direct Simulation of Gas Flows*. Clarendon.

Chen, C. L., Chakravarthy, S. R. & Hung, C. M. 1994 Numerical investigation of separated nozzle flows. *AIAA J.* **32**, 1836–1843.

Elizarova, T. G. & Chetverushkin, B. N. 1984 Numerical algorithm for simulation of gas dynamic flows. *Dokl. Akad. Nauk. SSSR* **279**, 80–83.

Elizarova, T. G. & Chetverushkin, B. N. 1988 Kinetically coordinated difference schemes for modelling flows of a viscous heat-conducting Gas. *J. Comput. Math. Math. Phys.* **28**, 64–75.

Elizarova, T. G. & Chirokov, I. A. 1999 Macroscopic model for gas with translational – rotational nonequilibrium. *Comput. Maths Math. Phys.* **39**, 135–146.

Elizarova, T. G., Graur, I. A. & Lengrand, J. C. 2001 Two-fluid computational model for a binary gas mixture. *Eur. J. Mech.* B/ *Fluids* **3**, 351–369.

Elizarova, T. G., Graur, I. A., Chpoun, A. & Lengrand, J. C. 1997 Comparison of continuum and molecular approaches for the flow around a perpendicular disk. In *Proc. 20th Intl Symp. on Shock Waves* (ed. B. Sturtevant), pp. 795–800. World Scientific.

Elizarova, T. G., Graur, I. A., Lengrand, J. C. & Chpoun, A. 1995 Rarefied gas flow simulation based on quasi-gasdynamic equations. *AAIA J.* **33**, 2316–2324.

Elizarova, T. G. & Sheretov, Yu. V. 2002 Analyse du probleme de l’ecoulement gazeoux dans les microcanaux par les equations quasi hidrodynamiques. *Congres de la Societe Hydrotechnique de France (SHF), “Microfluidique”, Toulouse, Decembre 2002*, pp. 309–318.

Frey, M. & Hagemann, G. 1998 Status of flow separation prediction in rocket nozzles. *AIAA Paper* 98-3619.

Goryainov, V. A. 2000 Origin of circulating zones in free supersonic jets. *Comput. Fluid Dyn. J.* **10**, 401–405.

Graur, I. A. 2001 Method of quasi-gasdynamic splitting for solving the Euler equations. *J. Comput. Maths Math. Phys.* **41**, 1506–1518.

Graur, I. A., Elizarova, T. G., Kudriashova, T. A., Polyakov, S. V. & Montero, S. 2002*a* Implementation of underexpanded jet problems on multiprocessor computer systems. In *Parallel Computational Fluid Dynamics, Practice and Theory* (ed. P. Wilders *et al.*), pp. 151–158. Elsevier.

Graur, I. A., Elizarova, T. G. & Lengrand, J. C. 1997 Quasigasdynamic equations with multiple translational temperatures. *Rep.* R97-1. Laboratoire d’Aerothermique du CRNS, Meudon, France, ISSN 0248451X.

Graur, I. A., Elizarova, T. G. & Lengrand, J. C. 1999 Numerical computation of shock wave configurations in underexpanded jets. *Rep.* R99-2. Laboratoire d'Aerothermique du CRNS, Meudon, France, ISSN 0248451X.

Graur, I. A., Elizarova, T. G., Ramos, A., Tejeda, G., Fernández, J. M. & Montero, S. 2002*b* Numerical and experimental investigation of shock waves in hypersonic axisymmetric jets. In *Shock Waves 2001, Proc. 23rd Intl Symp. on Shock Waves. Fort Worth, Texas, USA* (ed. F. K. Lu), pp. 993–1001.

Graur, I. A., Ivanov, M. S., Markelov, G. N., Burtschell, Y., Valerio, E. & Zeitoun, D. 2003 Comparison of kinetic and continuum approaches for simulation of shock wave/boundary layer interaction. *Shock Wave J.* **12**, 343–350.

Gribben, B. J., Cantarini, F., Badcock, K. J. & Richards, B. 1998 Numerical study of an underexpanded jet. In *Proc. Third Eur. Symp. on Aerothermodynamics for Space Vehicles. ESTEC*. ESA SP-426, pp. 111–118.

Hirschfelder, J. O., Curtiss, C. F. & Bird, R. B. 1954 *Molecular Theory of Gases and Liquids.* Wiley & Sons.

Lengrand, J. C., Chpoun, A., Graur, I. A. & Elizarova, T. G. 1995 Supersonic rarefied gas flow around a perpendicular disk. *Rep.* R95-6. Laboratoire d'Aerothermique du CNRS, Meudon, France, ISSN 0248451X.

Liepmann, H. W. & Roshko, A. 1957 *Elements of Gasdynamics.* Wiley & Sons.

Mason, P. J. & Sykes, R. I. 1979 Three-dimensional numerical integration of Navier-Stokes equations for the flow over surface-mounted obstacles. *J. Fluid Mech.* **91**, 433–450.

Maté, B., Graur, I. A., Elizarova, T., Chirokov, I., Tejeda, G., Fernández, J. M. & Montero, S. 2001 Experimental and numerical investigation of an axisymmetric supersonic jet. *J. Fluid Mech.* **426**, 177–197.

Miller, D. R. 1988 Free jet sources. In *Atomic and Molecular Beam Methods* (ed. G. Scoles), vol. I, pp. 14–53. Oxford University Press.

Montero, S., Maté, B., Tejeda, G., Fernández, J. M., & Ramos, A. 2000 Raman studies of free jet expansion. Diagnostics and mapping. In *Atomic and Molecular Beams. The State of the Art, 2000* (ed. R. Campargue), pp. 295–306. Springer.

Montero, S., Ramos, A., Tejeda, G., Fernández, J. M. & Maté, B. 2002 Diagnostic of hypersonic shock waves by Raman spectroscopy. In *Shock Waves 2001, Proc. 23rd Intl Symp. on Shock Waves, Fort Worth, Texas, USA* (ed. F. K. Lu), pp. 425–433.

Novopashin, S. A. & Perepelkin, A. L. 1989 Axial symmetry loss of a supersonic preturbulent jet. *Phys. Lett.* A **135**, 290–293.

Parker, J. G. 1959 Rotational and vibrational relaxation in diatomic gases. *Phys. Fluids* **2**, 449–462.

Perry, A. E. & Chong, M. S. 1987 A description of eddying motions and flow patterns using critical-point concepts. *Annu. Rev. Fluid Mech.* **19**, 125–155.

Quirk, J. J. 1994 A contribution to the greate Riemann solver debate. *Intl J. Numer. Meth. Fluids* **18**, 555–574.

Quirk, J. J. 1998 AMRITA- A computational facility for CFD modelling. *Lecture Notes prepared for VKI 29th CFD Lecture Series*, 23–27 February.

Ramos, A. 2001 Procesos de intercambio energético en expansiones supersónicas: estudio por espectroscopía Raman. Thesis, Universidad Complutense de Madrid (in Spanish).

Ramos, A., Maté, B., Tejeda, G., Fernández, J. M. & Montero, S. 2000 Raman spectroscopy of hypersonic shock waves. *Phys. Rev.* E **62**, 4940–4945.

Rebrov, A. K. 1985 Free jet as an object of nonequilibrium processes investigation. In *Proc. 13th Intl Symp. Rarefied Gas Dynamics* (ed. O. M. Belotserkovskii), vol. 2, pp. 849–864. Plenum Press.

Rebrov, A. K. & Chekmarev, S. F. 1971 The spherical expansion of a viscous heat conducting gas into a submerged space. *Prikl. Mekh. Tekhn. Fis.* **3**, 122–126 (in Russian).

Sheretov, Yu. V. 1997 Quasihydrodynamic equations as a model for viscous compressible heat conductive flows. In *Implementation of Functional Analysis in the Theory of Approaches.* Tver University, pp. 127–155 (in Russian).

Sheretov, Yu. V. 2000 *Mathematical Modeling of Gas and Liquid Flows based on Quasihydrodynamic and Quasigasdynamic Equations.* Tver University (in Russian).

Shevelev, Yu. D. 1986 *Spatial Problems of Computational Aero and Hydrodynamics.* Moscow, Nauka, (in Russian).

Shevelev, Yu. D. & Klekovkin, C. G. 2003 Numerical simulation of spatial detached viscous incompressible flows near a plate with an obstacle. *J. Math. Modelling*, to appear (in Russian).

Sreekanth, A. K., Prasad, A. & Prasad, D. 1991 Numerical and experimental investigations of rarefied gas flows through nozzles and composite systems. *Proc. 17th Intl Symp. Rarefied Gas Dynamics* (ed. A. E. Beylich), pp. 987–994.

Stenholm, T. & Jover, V. 1997 Flow separation control activities at Volvo and SEP. *ESA Advanced Nozzle Workshop, University of Rome, Italy, October 1997*.

Teshima, K. & Usami, M. 2001 DSMC calculation of supersonic expansion at a very large pressure ratio. In *Proc. 22nd Intl Symp. Rarefied Gas Dynamics*, *AIP Conf. Proc.* 585 (ed. T. J. Bartel & M. A. Gallis), pp. 737–744.

Volchkov, V. V., Ivanov, A. V., Kislyakov, N. I., Rebrov, A. K., Sukhnev, V. A. & Sharafutdinov, R. G. 1973 Low-density jets beyond a sonic nozzle at large pressure drops. *Zh. Prikl. Mekh. Tekhn. Fiz.* **2**, 64–73. English translation by Plenum Publishing Corporation, New York, 1975, pp. 200–207, UDC 532.522.2.

Welsh, F. P. 1997 Electron beam fluorescence measurements of shock reflection hysteresis in an underexpanded jet. In *21st Intl Symp. on Shock Waves*, *Great Keppel, Australia*, unpublished.